

# Numerical Simulation of Sound Generated by Vortex Pairing in a Mixing Layer

Christophe Bogey,\* Christophe Bailly,† and Daniel Juvé‡  
École Centrale de Lyon, 69131 Ecully, France

A numerical code solving the filtered Navier–Stokes equations is developed using special techniques of computational aeroacoustics. This approach allows a direct determination of the compressible field on a computational domain including the acoustic far field. A two-dimensional mixing layer between two flows at  $M_1 = 0.12$  and  $M_2 = 0.48$  is simulated. The Reynolds number built up from the initial vorticity thickness and the velocity difference across the mixing layer is  $Re_\omega = 1.28 \times 10^4$ . An appropriate forcing of the mixing layer is defined to have only one pairing in the computational domain at a fixed location. The sound generation pattern for a single pairing displays a double spiral structure, corresponding to the rotating quadrupole associated to two corotative vortices. Successive pairings produce an acoustic radiation at the frequency of this mechanism. The directly computed far-field sound is then compared to the prediction of Lighthill's acoustic analogy (Lighthill, M. J., "On Sound Generated Aerodynamically—I. General Theory," *Proceedings of the Royal Society of London*, Vol. 211, Series A 1107, 1952, pp. 564–587) based on the aerodynamic fluctuations provided by the large-eddy simulation code. Two integral formulations of the analogy, based on spatial derivatives and time derivatives, respectively, are tested. Results are in good qualitative agreement with the results of direct simulation. The accuracy is, however, greater with the formulation using time derivatives instead of spatial derivatives.

## I. Introduction

THE aim of computational aeroacoustics (CAA) is to calculate acoustic fluctuations generated by flows, to provide reliable predictions to reduce noise radiation. CAA imposes strong requirements,<sup>1,2</sup> which have led to the development of specific techniques, as compared with more classical computational fluid dynamics (CFD) methods. The challenge is to compute the small acoustic fluctuations very accurately to understand the mechanisms of noise generation.

Lighthill's analogy,<sup>3</sup> in 1952, was the starting point of modern aeroacoustics. In this approach, the acoustic field is obtained via a volume integral over the turbulent flow. The source terms can be built up from aerodynamic data determined by solving Navier–Stokes equations<sup>2,4</sup> or by generating a stochastic turbulent field.<sup>5</sup> In this method, the effects of flow on the propagation of acoustic waves, namely, convection and refraction, are neglected. Moreover, the explicit knowledge of the Green function is needed, which limits the application of this method to simple geometries.

The direct calculation of the acoustic field is an alternative and attractive method.<sup>1,2</sup> The compressible unsteady equations of flow motion are solved to provide both aerodynamic and acoustic variables, without restricting hypothesis and without modeling. Nevertheless, the direct approach has to face serious difficulties linked to the great disparity of scales and levels between the acoustic and aerodynamic fields. Acoustic perturbations are several orders of magnitude smaller than aerodynamic perturbations, and the ratio of aerodynamic disturbances to acoustic disturbances increases when the flow Mach number decreases. Characteristic length scales are also very different, for example, between the thickness of a mixing layer and the acoustic wavelength of the emitted sound. Finally, direct exploitation of the computed compressible field also requires the

use of accurate artificial boundary conditions to minimize acoustic reflections at the limits of the computational domain.

Direct simulation of noise can be based on each of the three CFD methods used to solve Navier–Stokes equations: direct numerical simulation (DNS), large-eddy simulation (LES), and unsteady Reynolds-averaged Navier–Stokes (RANS). These approaches have been adapted to exploit directly the compressible field by using CAA numerical techniques. For example, Colonius et al.,<sup>6</sup> Mitchell et al.,<sup>4,7</sup> Freund et al.,<sup>8</sup> and Freund<sup>9</sup> have performed DNS to compute the sound generated by a two-dimensional mixing layer, by axisymmetric jets, and by full three-dimensional jets, respectively. Mankbadi<sup>10</sup> has investigated supersonic axisymmetric jets using the large-scale equations, and Shen and Tam<sup>11</sup> have studied the generation of screech tones in axisymmetric jets with an unsteady RANS code. In LES, only larger scales are calculated, the smaller ones are modeled, whereas in DNS, all turbulent structures are described. Computation cost is then decreased compared to DNS, and LES is less limited to canonical flows at low Reynolds number. It is then natural to use LES to perform direct acoustic simulations.

Noise generation by vortex pairing in a medium at rest has been studied both theoretically<sup>12</sup> and numerically.<sup>13</sup> Colonius et al.<sup>6</sup> have investigated this noise mechanism in a two-dimensional mixing layer using DNS. The flow was forced at its fundamental frequency and its first three subharmonic frequencies so that two vortex pairings occurred at fixed streamwise locations. The acoustic radiation generated by the first pairings was found by filtering the compressible field at the pairing frequency.

In this paper, the noise radiated by vortex pairings in a subsonic bidimensional mixing layer is investigated using LES. Large, persistent, two-dimensional rollers have been observed in mixing layers by Brown and Roshko<sup>14</sup> and Winant and Browand.<sup>15</sup> These bidimensional structures are mainly found in the early stage of turbulent flow development. Three-dimensional effects appear downstream of the first few pairings. Experimentally, to isolate these two-dimensional structures and to study their role,<sup>16,17</sup> the mixing layers can be forced at the frequency corresponding to their natural rollup and its subharmonics.

In the same way, our two-dimensional mixing layer is forced at its fundamental frequency and at its first subharmonic frequency. Thus, a fixed source corresponding to the first pairing is obtained. The aim of our work is then not to calculate a full developed mixing layer, but to provide directly noise generated by vortex merging without filtering the sound field and to better understand this typical noise mechanism. The compressible field given by LES is also used as

Received 2 August 1999; revision received 1 April 2000; accepted for publication 13 April 2000. Copyright © 2000 by the authors. Published by the American Institute of Aeronautics and Astronautics, Inc., with permission.

\*Postdoctoral Student, Laboratoire de Mécanique des Fluides et d'Acoustique, UMR Centre National de la Recherche Scientifique 5509; christophe.bogey@ec-lyon.fr.

†Assistant Professor, Laboratoire de Mécanique des Fluides et d'Acoustique, UMR Centre National de la Recherche Scientifique 5509; christophe.bailly@ec-lyon.fr. Member AIAA.

‡Professor, Laboratoire de Mécanique des Fluides et d'Acoustique, UMR Centre National de la Recherche Scientifique 5509. Member AIAA.

reference solution to valid hybrid approaches. Two formulations of Lighthill's<sup>3</sup> analogy are applied using the velocity field provided by LES. This point is important because in many practical applications, only the aerodynamic velocity field is available using LES.

In this paper, we present the simulation techniques, as well as the results of acoustic radiation in a mixing layer. An LES code, ALESIA, is developed. Numerical techniques, and particularly the discretization scheme and boundary conditions, are introduced in Sec. II. Flow characteristics and simulation specifications are described in Sec. III, and the whole compressible field computed by LES is shown in Sec. IV. The noise mechanism associated to vortex pairing is described and discussed in relation to works on the noise generated by corotative vortices.<sup>12,13</sup> Two integral formulations of Lighthill's analogy<sup>3</sup> are applied in Sec. V. Concluding remarks are given in Sec. VI.

## II. Numerical Simulation Algorithm

### A. Governing Equations

The full Navier–Stokes equations for two-dimensional fluid motion are written in conservative form. In Cartesian coordinates, we have

$$\frac{\partial \mathbf{U}}{\partial t} + \frac{\partial Fe}{\partial x_1} + \frac{\partial Ge}{\partial x_2} - \frac{\partial Fv}{\partial x_1} - \frac{\partial Gv}{\partial x_2} = 0 \quad (1)$$

The variable vector  $\mathbf{U}$  is given by

$$\mathbf{U} = \begin{bmatrix} \rho \\ \rho u_1 \\ \rho u_2 \\ \rho e \end{bmatrix}$$

where  $\rho$ ,  $u_1$ ,  $u_2$ , and  $e$  are the density, the axial and radial velocity components, and the total specific energy, respectively. Fluxes are split into Euler fluxes  $Fe$  and  $Ge$  and viscous fluxes  $Fv$  and  $Gv$ . System (1) is completed by the definition of the total specific energy for a perfect gas

$$\rho e = [p/(\gamma - 1)] + \frac{1}{2}\rho(u_1^2 + u_2^2)$$

where  $\gamma$  is the specific heat ratio and  $p$  the pressure. Thus, Euler fluxes are written as

$$Fe = \begin{bmatrix} \rho u_1 \\ p + \rho u_1^2 \\ \rho u_1 u_2 \\ (\rho e + p)u_1 \end{bmatrix} \quad Ge = \begin{bmatrix} \rho u_2 \\ \rho u_1 u_2 \\ p + \rho u_2^2 \\ (\rho e + p)u_2 \end{bmatrix}$$

and viscous fluxes as

$$Fv = \begin{bmatrix} 0 \\ \tau_{11} \\ \tau_{12} \\ u_1 \tau_{11} + u_2 \tau_{12} \end{bmatrix} \quad Gv = \begin{bmatrix} 0 \\ \tau_{21} \\ \tau_{22} \\ u_1 \tau_{21} + u_2 \tau_{22} \end{bmatrix}$$

The viscous stress tensor  $\tau_{ij}$  is defined by  $\tau_{ij} = 2\mu S_{ij}$ , where  $\mu$  is the dynamic molecular viscosity and  $S_{ij}$  the deviatoric part of the deformation stress tensor given by

$$S_{ij} = \frac{1}{2} \left( \frac{\partial u_i}{\partial x_j} + \frac{\partial u_j}{\partial x_i} - \frac{2}{3} \delta_{ij} \frac{\partial u_k}{\partial x_k} \right)$$

### B. Numerical Scheme

Euler fluxes are primordial in acoustic phenomena because they supply both the nonlinear generation and the propagation of sound. As a result, they need to be discretized by an accurate numerical scheme, here we use the dispersing relation preserving (DRP) scheme of Tam and Webb<sup>18</sup>:

$$\left( \frac{\partial Fe}{\partial x} \right)_{i,j} = \frac{1}{\Delta x} \sum_{l=-3}^3 a_l Fe_{i+l,j}$$

Tam and Webb<sup>18</sup> chose the coefficients  $a_l$  of their space discretization by requiring that the effective wave number provided by the finite difference scheme be a close approximation to the actual wave number. This optimized fourth-order scheme displays very low dissipation and dispersion rates and allows acoustic propagation over large distances, with only six points per wavelength. The spatial discretization is combined with a fourth-order Runge–Kutta method<sup>19</sup> for time integration. This algorithm requires low storage and is stable up to a Courant–Friedrichs–Lewy (CFL) number

$$\text{CFL} = \min \left\{ \frac{c}{1+M} \frac{\Delta t}{\Delta x}, \frac{c \Delta t}{\Delta y} \right\}$$

equal to 1.73, where  $c$  is the speed of sound,  $M$  is the axial Mach number, and  $\Delta t$ ,  $\Delta x$ , and  $\Delta y$  are the time and space discretization steps. The viscous fluxes are discretized with a centered second-order finite difference scheme. They are integrated in the last step of the Runge–Kutta algorithm. This temporal discretization is sufficient for the mixing layer Reynolds number studied in the present study (see also Ref. 20). The viscous terms are very small compared to the convective terms. The CFL criterion for the viscous terms is also much higher than the criterion required for the convective terms. Thus, the time step is small enough so that the first-order temporal integration of the viscous terms is fairly accurate. Finally, Eq. (1) is advanced in time in the following way:

$$U_{i,j}^1 = U_{i,j}^n + \alpha_1 \Delta t Ke_{i,j}^n, \quad U_{i,j}^2 = U_{i,j}^n + \alpha_2 \Delta t Ke_{i,j}^1 \\ U_{i,j}^3 = U_{i,j}^n + \alpha_3 \Delta t Ke_{i,j}^2, \quad U_{i,j}^{n+1} = U_{i,j}^n + \alpha_4 \Delta t Ke_{i,j}^3 + \Delta t Kv_{i,j}^n$$

where  $Ke$  and  $Kv$  are the integration terms of the Euler and viscous fluxes defined by

$$Ke_{i,j}^k = - \sum_{l=-3}^3 a_l \left( \frac{1}{\Delta x} Fe_{i+l,j}^k + \frac{1}{\Delta y} Ge_{i,j+l}^k \right)$$

$$Kv_{i,j}^n = \frac{1}{2\Delta x} (Fv_{i+1,j} - Fv_{i-1,j}) + \frac{1}{2\Delta y} (Gv_{i,j+1} - Gv_{i,j-1})$$

The selective damping of Tam<sup>1</sup> is used to filter out numerical oscillations due to short waves not supported by the numerical scheme and generated by boundary conditions or grid stretching. As an example, the damping term added to system (1) in the axial direction is

$$\frac{\partial U}{\partial t} = \dots - \frac{c}{R_s \Delta x} \sum_{l=-3}^3 d_l (U_{i+l,j} - \bar{U}_{i+l,j})$$

where  $R_s$  is the stencil Reynolds number, usually<sup>1</sup>  $R_s = 5$ , and  $\bar{U}$  is the mean flow value. The coefficients  $d_l$  are chosen to damp only the short waves and not the long waves resolved accurately by the DRP scheme. These terms are integrated at the fourth step of the Runge–Kutta method, in the same way as the viscous terms.

### C. Boundary Conditions

The formulation of precise boundary conditions is very important for acoustic computations.<sup>1,2</sup> Spurious waves produced when fluctuations leave the computational domain must be minimized. Great care has then to be taken when using directly the acoustic field provided by Navier–Stokes calculations. Various formulations of boundary conditions and sponge zones have been tested before choosing the most accurate methods. Figure 1 shows the boundary conditions used on each side of the computational domain.

The nonreflecting boundary conditions of Tam and Dong<sup>21</sup> have been implemented. A better accuracy is obtained with this formulation than with the various approaches essentially based on characteristic equations.<sup>22</sup> Tam and Dong boundary conditions are built from the asymptotic expressions of Euler's equations in the acoustic far field. They are applied to three points, with DRP decentered schemes and are integrated with the Runge–Kutta algorithm.

When only acoustic fluctuations reach the boundary, that is, for inflow and lateral boundaries, the following radiation conditions are applied:

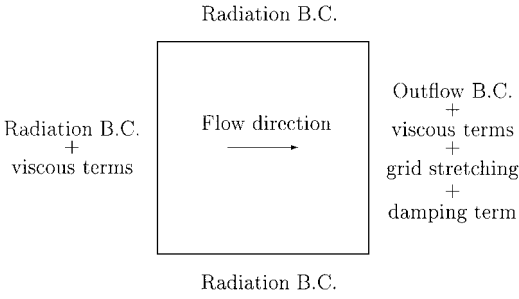


**Fig. 1** Boundary condition configuration for mixing layer simulations.

$$\frac{1}{V_g} \frac{\partial}{\partial t} \begin{bmatrix} \rho \\ u_1 \\ u_2 \\ p \end{bmatrix} + \left( \frac{\partial}{\partial r} + \frac{1}{2r} \right) \begin{bmatrix} \rho - \bar{\rho} \\ u_1 - \bar{u}_1 \\ u_2 - \bar{u}_2 \\ p - \bar{p} \end{bmatrix} = 0 \quad (2)$$

where  $V_g$  is the acoustic group velocity.<sup>21</sup> The mean density  $\bar{\rho}$ , velocity components  $\bar{u}_1$  and  $\bar{u}_2$ , and pressure  $\bar{p}$  are computed at each time step of the simulation. These quantities converge quickly to the steady-state solution. The mean velocity field of our forced mixing layer is displayed in the next section.

Outflow boundary conditions are also necessary when aerodynamic fluctuations have to leave the domain:

$$\begin{aligned} \frac{\partial \rho}{\partial t} + \bar{V} \cdot \nabla(\rho - \bar{\rho}) &= \frac{1}{\bar{c}^2} \left( \frac{\partial p}{\partial t} + \bar{V} \cdot \nabla(p - \bar{p}) \right) \\ \frac{\partial u_1}{\partial t} + \bar{V} \cdot \nabla(u_1 - \bar{u}_1) &= -\frac{1}{\bar{\rho}} \frac{\partial(p - \bar{p})}{\partial x} \\ \frac{\partial u_2}{\partial t} + \bar{V} \cdot \nabla(u_2 - \bar{u}_2) &= -\frac{1}{\bar{\rho}} \frac{\partial(p - \bar{p})}{\partial y} \\ \frac{1}{V_g} \frac{\partial p}{\partial t} + \frac{\partial(p - \bar{p})}{\partial r} + \frac{(p - \bar{p})}{2r} &= 0 \end{aligned} \quad (3)$$

where  $\bar{c} = \sqrt{(\gamma \bar{p} / \bar{\rho})}$  is the mean sound velocity.

These boundary conditions were successfully validated with the Institute for Computer Applications in Science and Engineering test cases,<sup>23</sup> that is, acoustic pulse and vortex convected by a uniform flow. However, the exit of vortical structures generates weak spurious acoustic waves, typically a few percent of the incoming perturbations. Unfortunately, these small parasitic waves are not negligible with respect to the sound field because of the difference of magnitude between aerodynamic and acoustic perturbations. A sponge zone has been built to dissipate aerodynamic fluctuations before they reach the outflow boundary. Two methods are combined following Colonius et al.<sup>24</sup> First, the mesh is stretched in the axial direction so that the turbulent structures are not supported by the numerical scheme. Second, a damping term is added in the equations to avoid the upstream propagation of spurious reflections produced in the sponge region. Many damping terms have been introduced in CAA, and one of the most popular is the perfectly matched layer proposed by Bérenger.<sup>25</sup> In the current study, fluctuations and reflected waves are damped by using the following additional term in system (1):

$$\frac{\partial U}{\partial t} = \dots - \frac{c \sigma(x, y)}{\Delta x} (U - \bar{U}) \quad (4)$$

with

$$\sigma(x, y) = \sigma_{\max} \left( \frac{x - x_o}{x_{\max} - x_o} \right)^2$$

where  $\sigma_{\max} = 0.15$  and  $x_o$  and  $x_{\max}$  are the locations of the beginning and of the end of the damping zone. Viscous fluxes are also integrated in inflow and outflow boundaries, to avoid discontinuity in the viscous terms.

#### D. Subgrid Scale Model

In DNS, all turbulent scales have to be calculated. This is often difficult with the computer resources available and restricts DNS applications to low Reynolds number flows.

LES is an alternative for computing flows at higher Reynolds number. In this technique, only the larger structures are computed, and the effects of smaller scales are taken into account via a subgrid-scale model. A turbulent viscosity  $\mu_t$  ensures dissipation of the smaller unresolved structures. Basically,  $\mu$  is replaced by  $\mu + \mu_t$  in Eq. (1). Various models have been built to determine an expression of this turbulent viscosity. To keep the problem as simple as possible for aerodynamics, we choose Smagorinsky's model<sup>26</sup>

$$\mu_t = \rho (C_s \Delta_c)^2 \sqrt{2 S_{ij} S_{ij}}$$

where the Smagorinsky constant is taken to be  $C_s = 0.18$ , and the characteristic grid length is  $\Delta_c = \sqrt{(\Delta x \Delta y)}$ . More sophisticated subgrid scale models could be used.<sup>27,28</sup>

### III. Flow Simulation

#### A. Flow Parameters

A two-dimensional mixing layer is defined by the following inflow hyperbolic-tangent velocity profile, as shown in Fig. 2:

$$u_1(y) = \frac{U_1 + U_2}{2} + \frac{U_2 - U_1}{2} \tanh \left[ \frac{2y}{\delta_o(0)} \right]$$

where  $U_1$  and  $U_2$  are the velocities of the slow and rapid flows, respectively, and  $\delta_o(0)$  is the initial vorticity thickness. One also defines the convection velocity as  $U_c = (U_1 + U_2)/2 = 0.3c$ , where  $U_1 = 0.12c$  and  $U_2 = 0.48c$ . The velocity difference is moderate between the two flows because the relative convection Mach number is  $M_c = (U_2 - U_1)/(2c) = 0.18$ .

The Reynolds number based on the initial vorticity thickness is equal to  $Re_\omega = \delta_o(0)(U_2 - U_1)/\nu = 1.28 \times 10^4$ . With the computational mesh described in the next section, this Reynolds number limits the subgrid-scale model viscosity to reasonably low values, as shown in Fig. 3. This indicates that the large structures are then well discretized and that their behavior is well represented by the filtered equations.

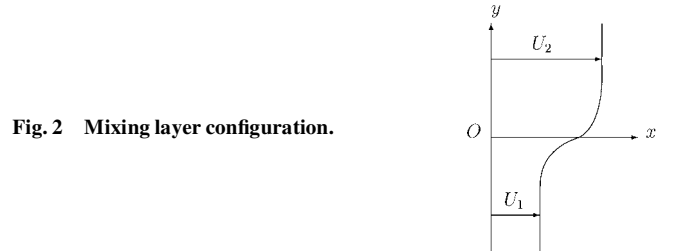


**Fig. 2** Mixing layer configuration.

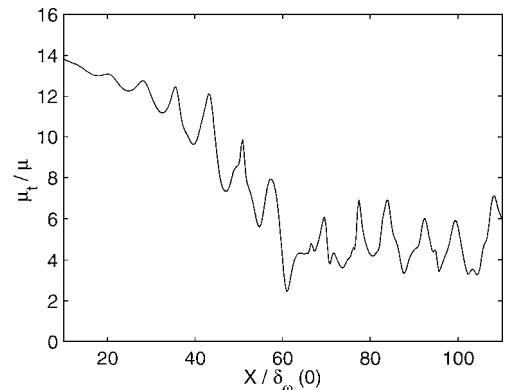


**Fig. 3** Ratio between turbulent viscosity and molecular viscosity at  $Y = 0$  in the axial direction; the mixing layer is forced at its fundamental frequency  $f_0$  and its first subharmonic.

## B. Numerical Specifications

The computational mesh has  $441 \times 441$  points. Minimum mesh spacing in the axial and radial directions are  $\Delta x_0 = 0.32\delta_0(0)$  and  $\Delta y_0 = 0.16\delta_0(0)$ . Grid points are concentrated in the shear zone, and mesh stretching is 1.8% on each side of this zone in the radial direction, up to the last 55 points, where  $\Delta y_{\max} = 3\delta_0(0)$ . Mesh spacing is constant in the axial direction, except for the last 100 points, where a 2.8% stretching is applied to form the sponge layer. The damping term (4) is added with a parabolic profile from  $X = 130\delta_0(0)$  to the outflow boundary at  $X = 270\delta_0(0)$ . A radial weighting of this term is also applied to make it zero outside the mixing layer. In this way, the sponge zone dissipates vortices in the mixing layer but not the acoustic radiation outside because the acoustic wavelength is large enough to be still supported by the stretched mesh. Finally, the physical portion of the computational domain extends to  $200\delta_0(0)$  in the axial direction and from  $-300\delta_0(0)$  up to  $300\delta_0(0)$  in the radial direction.

The time step is defined by  $\Delta t = \Delta y_0/c$ . The simulation runs for  $10^4$  iterations and is 1 h long on a C-98 Cray ( $1.6 \times 10^{-6}$  s per grid point and per iteration, and a CPU speed of 500 million floating-point operations).

## C. Inflow Forcing and Aerodynamic Results

Several experiments have demonstrated the importance of large coherent structures in turbulence,<sup>14,15,29</sup> and this is particularly true for flows at low to moderate Reynolds number. Crow and Champagne<sup>29</sup> have also shown that large structures can exhibit organized behavior when subjected to a suitable excitation.

To govern the development of the mixing layer, an excitation is introduced into the inflow. The flow is forced around the inflexion point of the profile by adding vortical perturbations to velocity components at every iteration. An harmonic excitation with pulsation  $\omega$  is defined as

$$u_1(x, y, t) = u_1(x, y, t) + [(y - y_0)/\Delta y_0]E \sin(\omega t)$$

$$u_2(x, y, t) = u_2(x, y, t) - [(x - x_0)/\Delta x_0]E \sin(\omega t)$$

where  $x_0$  and  $y_0$  are the location of the excitation, and  $E$  is the Gaussian weighting defined by

$$E = \alpha U_c \exp\left\{-\ln(2)\left[(x - x_0)^2 + (y - y_0)^2\right]/\Delta y_0^2\right\} \quad (5)$$

Actually, the mixing layer flow is forced at two frequencies: its fundamental frequency  $f_0$  and its first subharmonic  $f_0/2$ . The fundamental frequency corresponds to the most amplified instabilities, predicted by the linear theory of Michalke,<sup>30</sup> and is given by

$$f_0 = 0.132[U_c/\delta_0(0)]$$

This kind of excitation allows us to control the pairing process in the mixing layer<sup>6,20</sup> by adjusting the relative amplitude of the two coefficients  $\alpha$  in expression (5). The value of the coefficient  $\alpha$  is around  $5 \times 10^{-4}$  for the fundamental and  $2.5 \times 10^{-4}$  for the first subharmonic frequency, with a phase difference of  $\pi/2$ . The two amplitudes of the excitation are weak enough not to produce significant spurious acoustic waves.

As shown in Fig. 4, vortex pairings occur at a frequency equal to  $f_0/2$  and at a fixed position around  $X = 70\delta_0(0)$ . The numerical solution is in agreement with experimental visualizations of Winant and Browand,<sup>15</sup> who have described the vorticity field associated

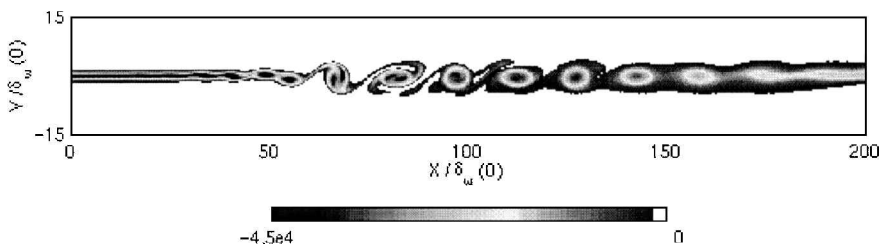


Fig. 4 Vorticity field computed by exciting the mixing layer at the two frequencies  $f_0$  and  $f_0/2$ , levels given in  $s^{-1}$ .

with vortex pairing in a mixing layer. The sponge zone is effective from  $X = 150\delta_0(0)$  and dissipates vortices before other pairings happen downstream. There are then no secondary significant sound sources after the first pairing. Figure 5 shows the mean streamwise velocity field calculated by LES and used in the formulation of boundary conditions (2) and (3). Near the pairing location around  $70\delta_0(0)$ , the layer thickness  $\delta_0$  doubles.

A broadband excitation has also been applied to simulate the natural development of the mixing layer. The linear spatial growth, turbulence rates, and spectra are not shown in this paper, but they conform to previous similar studies.<sup>14,20,31</sup>

## IV. Direct Calculation of the Acoustic Field

Vortex pairing can be described as two structures rotating around each other before sudden merger. Previous works<sup>15</sup> suggested that this typical nonlinear phenomenon constitutes a major acoustic source in subsonic flows, but there is no general agreement on this point.<sup>32</sup> However, in low Reynolds number flows, fine-scale turbulence does not play a fundamental role, and vortex pairing can be regarded as the dominant noise source.

The first simulation of noise radiated by a mixing layer ( $U_1 = c/4$ ,  $U_2 = c/2$ ,  $Re_\omega = 250$ ) was carried out by Colonius et al.<sup>6</sup> They have shown that vortex pairing generates a downstream acoustic radiation, with a wavelength in accordance with the frequency of pairings  $f_p = f_0/2$ . Therefore, we can expect in our simulation to find an acoustic frequency of  $f_p$ , corresponding to an acoustic wavelength equal to  $\lambda_p = 51.5\delta_0(0)$  in a medium at rest.

Figure 6 shows the dilatation field  $\Theta = \nabla \cdot \mathbf{u}$  calculated by ALE-SIA on the whole computational domain and related to the pressure in the uniform flows by

$$\Theta = \nabla \cdot \mathbf{u} = -\frac{1}{\rho_0 c_0^2} \left( \frac{\partial p}{\partial t} + U_i \frac{\partial p}{\partial x} \right), \quad i \in [1, 2] \quad (6)$$

Wave fronts are observed coming from the location of the pairings. The acoustic wavelength is comparable to  $\lambda_p$ , as expected. However, this wavelength is modulated by convection effects induced by the upper and lower flows. The wave fronts have a typical oval form, which is especially visible for the upper high-velocity flow. Acoustic radiation is well marked in the downstream direction and even more precisely for angles close to  $\theta_1 \approx 70$  deg for the lower flow and  $\theta_2 \approx 50$  deg for the upper flow, as shown in Fig. 7. The difference between the two directivities can also be attributed to convection effects.

Levels of the dilatation field are around  $2 s^{-1}$ , corresponding to 10 Pa for the pressure field. This value is small compared to the aerodynamic pressure fluctuations, which are greater than 1000 Pa. This result validates the efficiency of the boundary conditions because no spurious waves can be detected in the compressible field.

Figure 8 shows four views of the pairing zone. The vorticity field is superimposed on the dilatation field on the shear layer. The views

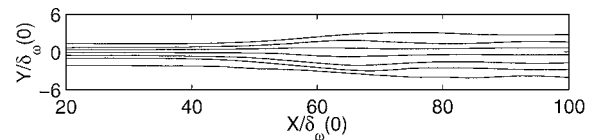


Fig. 5 Isolines of the longitudinal mean velocity provided by LES, defined for Mach 0.13, 0.15, 0.2, 0.3, 0.4, 0.45, and 0.47; in lower part, slow flow at Mach 0.12; and in upper part, rapid flow at Mach 0.48.

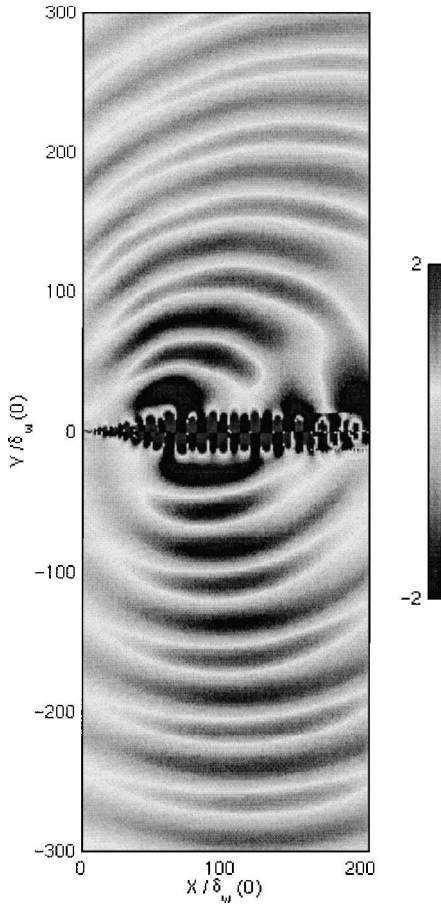


Fig. 6 Dilatation field  $\Theta = \nabla \cdot u$  computed on the whole calculation domain, levels given in  $s^{-1}$ .

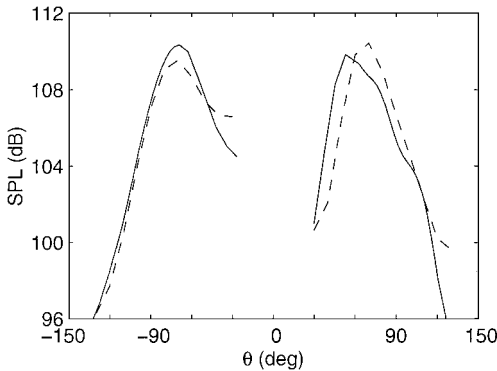


Fig. 7 Sound pressure directivity at a distance of  $100\delta_w(0)$  from the noise source located at  $X = 70\delta_w(0)$  and  $Y = 0$ : —, direct calculation of the sound, and - - -, time derivative formulation of the Lighthill analogy. Levels provided by the Lighthill analogy are scaled to compare the two patterns.

are regularly spaced over a period  $T_p = 1/f_p$ , defined as the time between two subsequent vortex pairings, and the cycle Figs. 8a–8d to Fig. 8a describes a pairing period. These views allow us to propose the noise generation mechanism associated to vortex pairing.

A double spiral structure with four lobes is observed, in particular in Fig. 8b. The analytical work of Powell<sup>12</sup> and numerical simulations of Mitchell<sup>13</sup> dealing with the noise generated by two corotative vortices present a similar radiation pattern. Powell<sup>12</sup> has identified this source as a rotating quadrupole.

We can detail the different steps of a pairing. In Fig. 8a, two neighboring vortices begin to roll around each other: This is the starting point of acoustic radiation. In Fig. 8b, a second radiation lobe appears perpendicular to the first one, which is now represented as a single dark spiral. The first lobe stops emitting and is succeeded

by the radiation of the second one in Fig. 8c. Finally, the second light lobe also stops emitting in Fig. 8d, and in Fig. 8a the two vortices are completely merged, while a new pairing process begins.

As shown by the simulations of Mitchell et al.,<sup>13</sup> vortex pairing generates sound during the rotation of the two vortices. A peak in amplitude is reached when the two vortices coalesce, and the amplitude diminishes significantly after merger. In our case, emission time associated to a vortex pair lasted for a pairing period  $T_p$ . Thus, the subsequent pairings are perfectly matched. Indeed, no discontinuity can be observed between wave fronts produced by successive pairings (there is discontinuity when emission time is smaller than a pairing period), and the radiations of two pairings cannot interfere (there is interference when emission time is greater than a pairing period).

This absence of interference is because sources travel over a very small distance during the pairing. The two fronts radiated by a vortex pairing appear to come from two very close locations. In Fig. 6, the darker and lighter fronts are not exactly concentric, the darker fronts being emitted a little upstream.

Furthermore, acoustic wavelength is directly connected to the rotation speed of the two vortices. To produce acoustic radiation with a wavelength provided by the pairing frequency  $f_p$ , the rotation speed must correspond to half this frequency because of the symmetry of the quadrupolar source. In other words, vortices complete half a revolution during the pairing period  $T_p$ . This is shown by Fig. 9, representing the vorticity field, and more precisely the successive orientations of the vortex pair at the four times defined in Fig. 8. During the time  $T_p/4$  between two views, the vortex pair completes one-eighth of a revolution. Figure 9d displays side by side, the two opposite orientations of the vortex pair before and after a period  $T_p$ .

The dynamics of pairings is then at the origin of the regular wave front pattern with no interference. The acoustic wavelength is given by the pairing frequency  $f_p$  because the corotative vortex pair completed half a rotation during each pairing period. Refraction effects can also be invoked to explain the radiation pattern. However, the shear layer thickness is very small compared to the acoustic wavelength, and we can therefore expect refraction to be of small importance.

## V. Lighthill's Acoustic Analogy

In this section, Lighthill's<sup>3</sup> analogy is applied using LES aerodynamic fluctuations. Two integral formulations of the analogy are used to estimate their respective accuracies.

### A. Theory

Lighthill<sup>3</sup> rearranges the mass and momentum equations to obtain

$$\frac{\partial^2 p'}{\partial t^2} - c_0^2 \Delta p' = \frac{\partial^2 T_{ij}}{\partial x_i \partial x_j}$$

where  $c_0$  is the ambient sound speed and  $T_{ij}$  is Lighthill's stress tensor defined as

$$T_{ij} = \rho u_i u_j + (p' - \rho' c_0^2) \delta_{ij} - \tau_{ij}$$

which can be approximated for flows at ambient temperature by  $T_{ij} \approx \rho u_i u_j$ . Outside the flow region,  $p' = \rho - \bar{\rho}$  reduces to the fluctuating acoustic density  $\rho' = p'/c_0^2$ , and  $T_{ij}$  is zero. Lighthill's equation can be interpreted as a wave equation in a medium at rest with a source term of quadrupolar nature and induced by the flow Reynolds stresses.

The solution of Lighthill's equation is obtained by using the three-dimensional free space Green's function,  $G(\mathbf{x}, t) = \delta(t - x/c_0)/(4\pi c_0^2 x)$  and takes the form of a retarded potential formulation. A solution involving space derivatives of  $T_{ij}$  and valid both in the near and far acoustic field is

$$p'(\mathbf{x}, t) = \frac{1}{4\pi} \int_V \frac{1}{r} \frac{\partial^2 T_{ij}}{\partial y_i \partial y_j} \left( \mathbf{y}, t - \frac{r}{c_0} \right) dy \quad (7)$$

where  $r = |\mathbf{x} - \mathbf{y}|$ . It is then possible to compute the acoustic pressure field, if the aerodynamic field is known, by calculating this integral over a volume  $V$  including all of the sources.

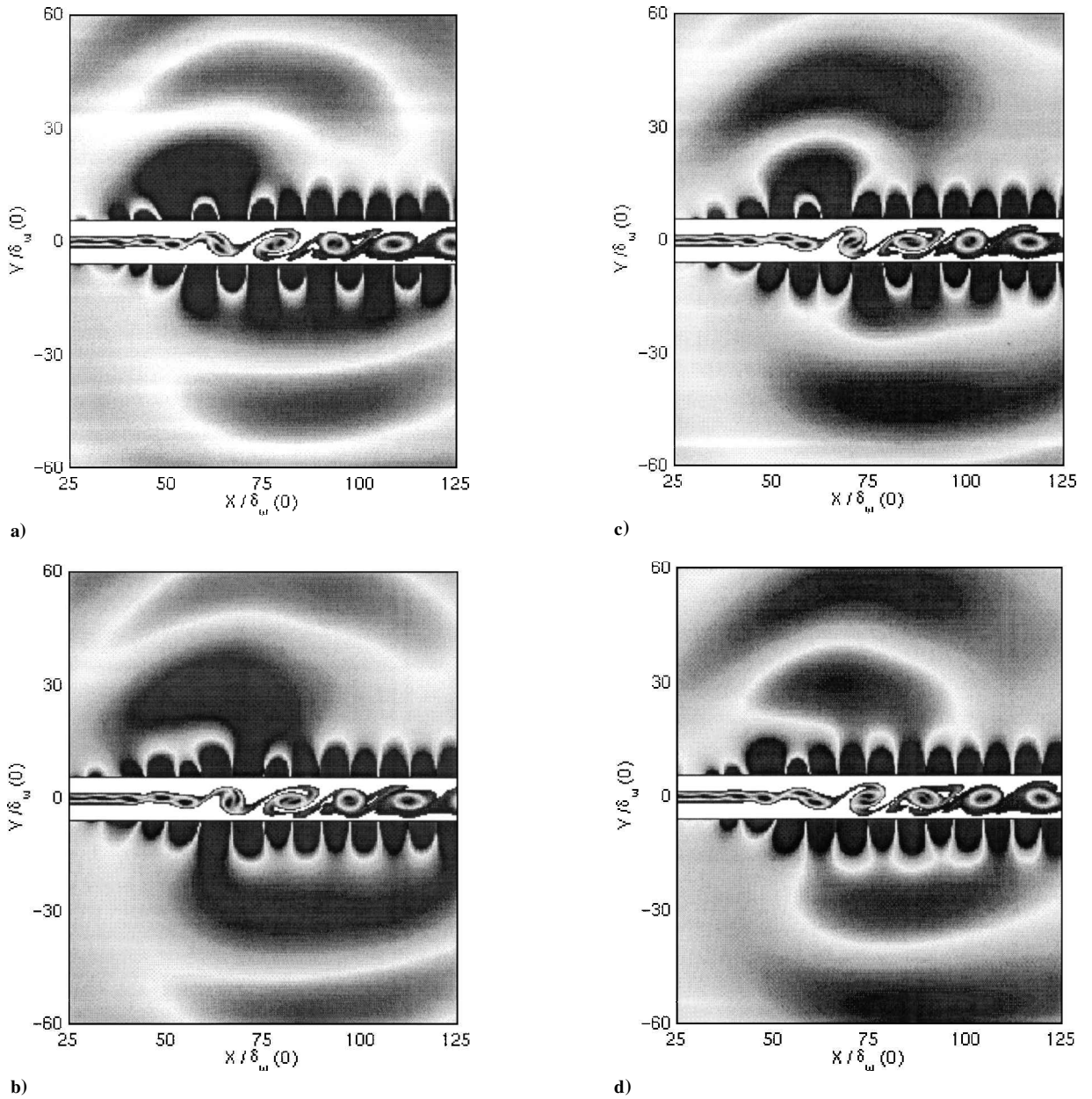


**Fig. 8** Four views of the vortex pairing zone: vorticity field in the mixing layer, surrounded by dilatation field; time step is  $T_p/4$  between two successive views. Cycle a)-b)-c)-d)-a) describes a pairing period.

Developments of the analogy have led to other expressions, described, for example, in a classical paper by Crighton.<sup>33</sup> In particular, a time derivative formulation can be written in the acoustic far field

$$p'(x, t) = \frac{1}{4\pi c_0^2} \int_V \frac{r_i r_j}{r^3} \frac{\partial^2 T_{ij}}{\partial t^2} \left( y, t - \frac{r}{c_0} \right) dy \quad (8)$$

This expression is more often used than expression (7) because it is less sensitive to the precise evaluation of the retarded time. Sarkar and Hussaini<sup>34</sup> have found that the use of space derivatives induces numerical errors of  $\mathcal{O}(1/M^2)$  with respect to formulation (8), where  $M$  is the convection Mach number of the acoustic sources. Thus, application of expression (7) to low Mach number flows requires a high-order scheme for interpolation of the retarded time value of the source term.

## B. Numerical Results

The two integral formulations (7) and (8) have been tested with the mixing layer simulated in Sec. III. They can not be applied without numerical adjustments, and storage and memory requirements are significant. Aerodynamic fluctuations given by LES are used to build the source terms. They are recorded every 10th aerodynamic

time step, which is equivalent to  $T_0/16 = T_p/32$ , where  $T_0 = 1/f_0$ . The source terms are stored during 540 acoustic time steps, corresponding to 16 pairing periods among the 36 pairing periods of the whole computation. The storage of each source term needs around 250 megaoctets. The source volume extends from 3 to  $229\delta_w(0)$  in the axial direction and from  $-53$  to  $53\delta_w(0)$  in the radial direction.

In Figs. 10 and 11, the terms  $\partial^2 T_{ij} / \partial y_i \partial y_j$  and  $\partial^2 T_{12} / \partial t^2$  are represented at the location defined by  $X = 70\delta_w(0)$  and  $Y = 0$ , that is, in the pairing zone. Both are periodic with a period of  $2T_0 = T_p$ . They also show high-frequency oscillations, which are recurrent and then correspond to physical mechanisms. The time recording step is small enough to take into account these oscillations, but a time interpolation is needed to minimize the error in the evaluation of source terms at the retarded time. Interpolation is performed with a fourth-order scheme using Lagrange polynomials. The two source terms are also quite different. The spatial source is more regular, whereas peaks in the temporal one are more pronounced. Because formulation (7) builds the acoustic field only with the retarded time, one can understand it is more sensitive than formulation (8) to errors in retarded time. Indeed, the quadrupolar nature of the source is only found through careful evaluation of retarded time.

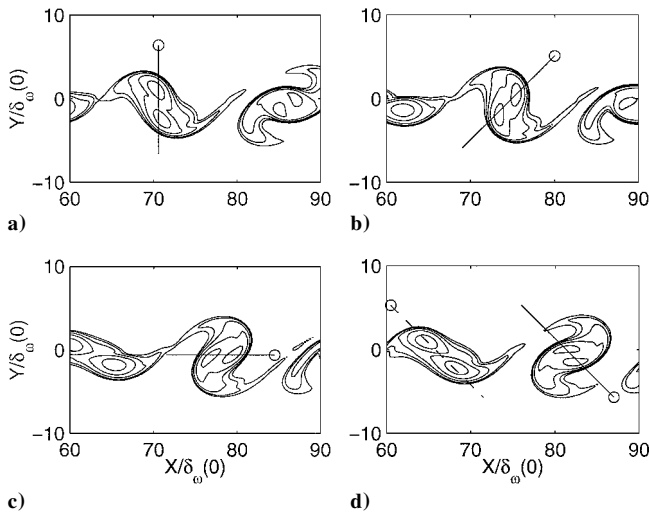


Fig. 9 Four snapshots of the vorticity field in the pairing region at the four times of Fig. 8; five isolines of vorticity are defined from  $-250$  to  $-4 \times 10^4 \text{ s}^{-1}$  following a geometrical ratio of 2:  $\text{---}\circ$ , orientation of two corotative vortices and  $\text{---}\ominus$ , orientation of the next vortices.

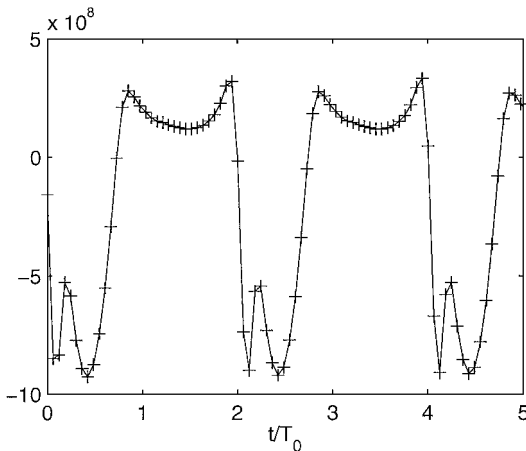


Fig. 10 Time evolution of the source term  $\partial^2 T_{ij} / \partial y_i \partial y_j$  at the point  $[X = 70\delta_\omega(0), Y = 0]$ ; time recordings are represented by crosses; dimensional source term.

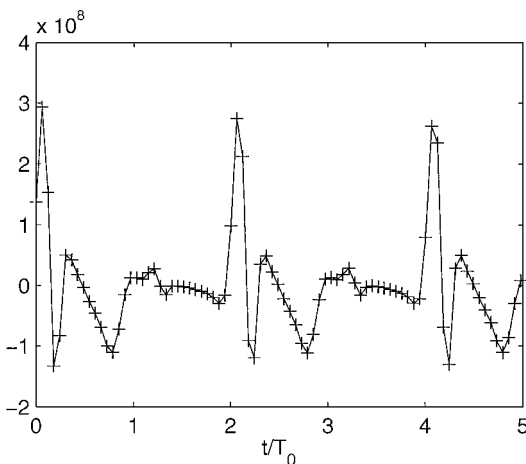


Fig. 11 Time evolution of the source term  $1/c_0^2 \partial^2 T_{12} / \partial t^2$  at the point  $[X = 70\delta_\omega(0), Y = 0]$ ; time recordings are represented by crosses; dimensional source term.

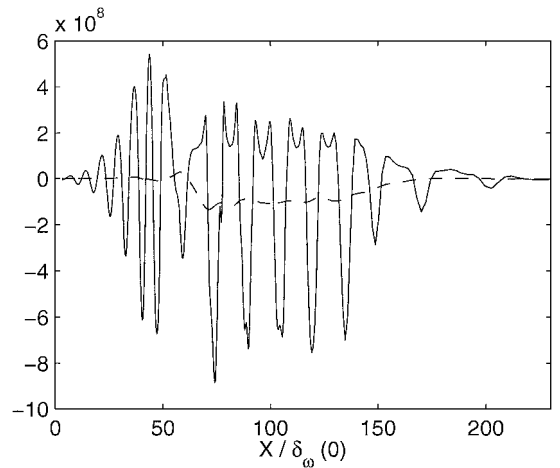


Fig. 12 Axial profile of the source term:  $\text{---}$ , source term  $\partial^2 T_{ij} / \partial y_i \partial y_j$ , and  $\text{---}$ , mean value of this term; dimensional source term.

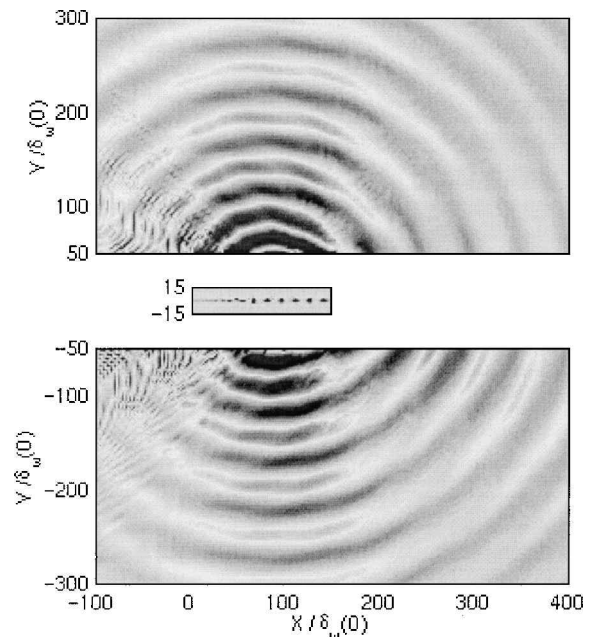


Fig. 13 Pressure field calculated by the Lighthill spatial derivatives formulation; arbitrary color scale.

The turbulent source volume is weighted to remove fluctuations on the outflow boundary, and to avoid discontinuity in source terms. Figure 12 shows the axial weighted profile of  $\partial^2 T_{ij} / \partial y_i \partial y_j$ . The doubling of the period appears clearly after the pairing mechanism. It also appears necessary to calculate and subtract the average of the source term in expression (7) to obtain centered pressure fluctuations. The space source term is then given by

$$\frac{\partial^2 T_{ij}}{\partial y_i \partial y_j} - \overline{\frac{\partial^2 T_{ij}}{\partial y_i \partial y_j}}$$

The mean value cannot be neglected, as shown in Figs. 10 and 12. For formulation (8), time derivatives naturally remove the mean source term.

Radiation predictions are presented in Figs. 13 and 14. Results of the two integral formulations are quite similar in phase and in level. However, formulation (8) seems more accurate than formulation (7), as pointed out by Sarkar and Hussaini.<sup>34</sup> With the spatial formulation, errors are produced in the upstream direction.

Formulas (7) and (8) of Lighthill's<sup>3</sup> analogy are based on the three-dimensional Green function  $e^{ik_0 r} / r$ . However, in our case we expect that the two-dimensional and three-dimensional sound fields will have the same radiation pattern and that only the levels will not

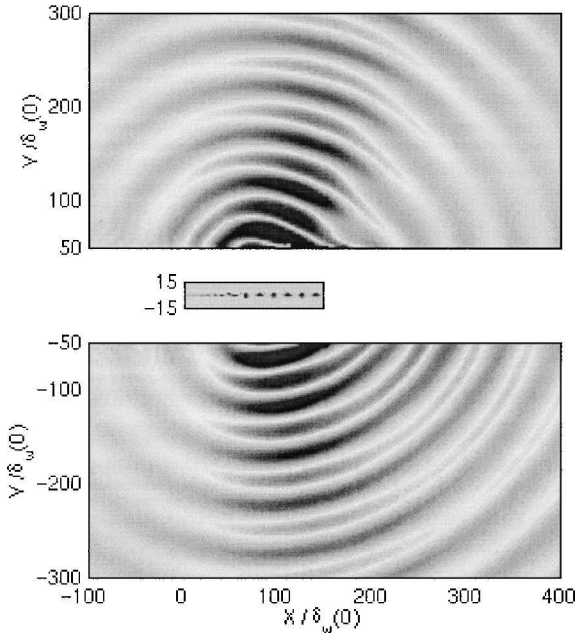


Fig. 14 Pressure field calculated by the Lighthill time derivatives formulation; color scale is the same as in Fig. 13.

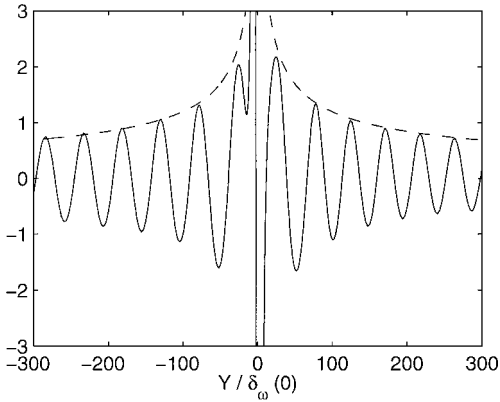


Fig. 15 Dilatation profile at  $X = 70\delta_{\omega}(0)$  in the radial direction provided by the direct calculation: --- represents a  $1/\sqrt{Y}$  decay; levels given in  $s^{-1}$ .

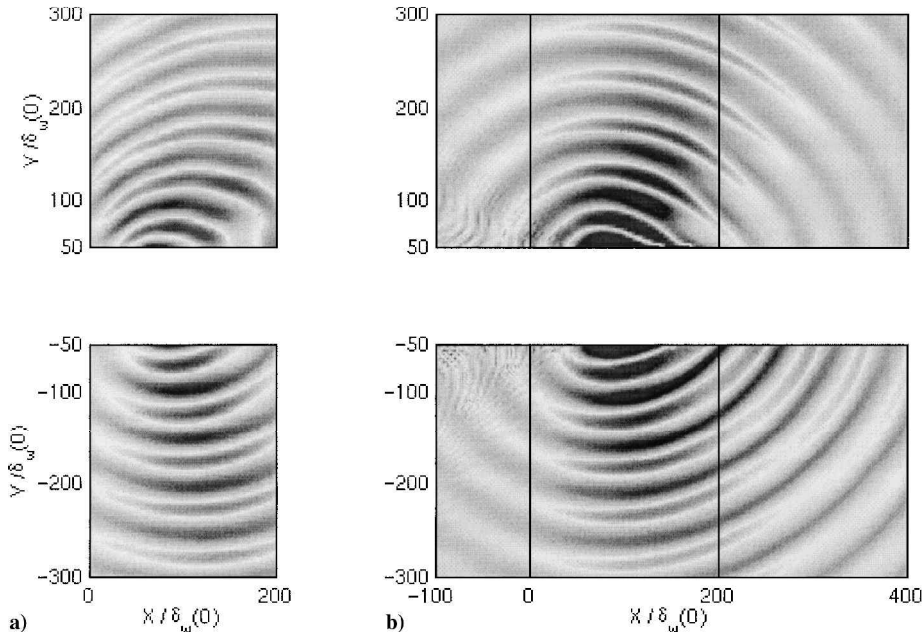


Fig. 16 Dilatation field provided at the same time by a) LES and b) time-derivative formulation of the Lighthill analogy.

be significant. Indeed, the two-dimensional Green function is given in Fourier space by

$$G(\mathbf{r}, \omega) = (1/4i)H_0^{(1)}(k_0 r)$$

where  $k_0 = \omega/c_0$  and  $H_0^{(1)}$  is the zeroth-order Hankel function. For  $k_0 r \geq 4$ , the Green function can be approximated as

$$G(\mathbf{r}, \omega) \approx (1/4i)\sqrt{2/\pi k_0 r} \exp(ik_0 r - i\pi/4)$$

The radiated acoustic field is basically harmonic at the pairing frequency  $f_p$ . Thus,  $k_0 r \geq 4$  with  $k_0 = 2\pi/\lambda_p$  and  $\lambda_p = 51\delta_{\omega}(0)$  correspond to a distance  $r \geq 32\delta_{\omega}(0)$ . Thus the two-dimensional Green function has the same behavior as the three-dimensional Green function with a phase delay and a decay of the acoustic field as  $1/\sqrt{r}$  instead of  $1/r$  in three dimensions, as shown in Fig. 15.

The two formulations (7) and (8) of Lighthill's<sup>3</sup> analogy provide radiation patterns in good agreement with the direct calculation. Refraction effects seems small in the direct calculation, and the radiation pattern is mainly associated to the noise generation mechanism. More precisely, Fig. 16 shows the dilatation field provided by the direct computation and the dilatation field  $\Theta$  obtained from the formulation (8) of Lighthill's analogy at the same time. Relation (6) is used for a medium at rest to determine the dilatation field provided by the Lighthill analogy. In the slow, lower flow, dilatation fields are similar, whereas wave fronts are affected by convection effects in the rapid, upper flow. As pointed out in the earlier discussion on the two-dimensional Green function, a constant phase delay is observed between the two calculations. Figure 7 compares the associated sound directivities. The acoustic radiation predicted by Lighthill's analogy shows symmetrical lobes for angles close to 70 deg from the downstream direction. The direct calculation takes into account all mean flow effects on sound propagation. As a result, Lighthill's analogy compares more favorably in the slow flow than in the rapid flow, where the acoustic peak is shifted downstream in the direct calculation.

## VI. Conclusions

A two-dimensional subsonic mixing layer is simulated to investigate its acoustic radiation. Noise is computed from LES using two approaches. In the first one, the sound field is provided directly by solving Navier–Stokes equations, and in the second one, Lighthill's<sup>3</sup> analogy is applied to determine the acoustic radiation pattern from the aerodynamic data.

Vortex pairings generate noise only with the frequency of pairings. Furthermore, the successive pairing radiations are matched without discontinuity and interference. The generation pattern is typical of a rotating quadrupole. This noise mechanism has been already shown in the case of two isolated identical vortices. Here, vortices are embedded in an external shear flow, which corresponds to a more general configuration.

Radiation patterns provided by Lighthill's<sup>3</sup> analogy are in good qualitative agreement with the directly computed acoustic far field, despite the absence of convection and refraction effects. The integral formulation using a time derivative is found to be more accurate than the formulation using a spatial derivative.

Direct acoustic calculation is an attractive method to understand noise generation because it supplies simultaneously turbulence and sound field data. It allows also an estimate of the accuracy of hybrid or analogical methods.

### Acknowledgments

The first author wishes to acknowledge financial support from Électricité de France, Direction des Études et Recherches (Philippe Lafon), and Centre National de la Recherche Scientifique (CNRS). Supercomputing time was provided by the Institut du Développement et des Ressources en Informatique Scientifique-CNRS.

### References

- <sup>1</sup>Tam, C. K. W., "Computational Aeroacoustics: Issues and Methods," *AIAA Journal*, Vol. 33, No. 10, 1995, pp. 1788–1796.
- <sup>2</sup>Lele, S. K., "Computational Aeroacoustics: A Review," AIAA Paper 97-0018, Jan. 1997.
- <sup>3</sup>Lighthill, M. J., "On Sound Generated Aerodynamically—I. General Theory," *Proceedings of the Royal Society of London*, Vol. 211, Series A 1107, 1952, pp. 564–587.
- <sup>4</sup>Mitchell, B. E., Lele, S. K., and Moin, P., "Direct Computation of the Sound Generated by Vortex Pairing in an Axisymmetric Jet," *Journal of Fluid Mechanics*, Vol. 383, 1999, pp. 113–142.
- <sup>5</sup>Bailly, C., Lafon, P., and Candel, S., "A Stochastic Approach to Compute Noise Generation and Radiation of Free Turbulent Flows," CEAS/AIAA Paper 95-092, June 1995.
- <sup>6</sup>Colonus, T., Lele, S. K., and Moin, P., "Sound Generation in a Mixing Layer," *Journal of Fluid Mechanics*, Vol. 330, 1997, pp. 375–409.
- <sup>7</sup>Mitchell, B. E., Lele, S. K., and Moin, P., "Direct Computation of Mach Wave Radiation in an Axisymmetric Supersonic Jet," *AIAA Journal*, Vol. 35, No. 10, 1997, pp. 1574–1580.
- <sup>8</sup>Freund, J. B., Lele, S. K., and Moin, P., "Direct Simulation of a Mach 1.92 Jet and Its Sound Field," AIAA Paper 98-2291, June 1997.
- <sup>9</sup>Freund, J. B., "Acoustic Sources in a Turbulent Jet: A Direct Numerical Simulation Study," CEAS/AIAA Paper 99-1858, May 1999.
- <sup>10</sup>Mankbadi, R. R., "Review of Computational Aeroacoustics in Propulsion Systems," *Journal of Propulsion and Power*, Vol. 15, No. 4, 1999, pp. 504–512.
- <sup>11</sup>Shen, H., and Tam, C. K. W., "Numerical Simulations of the Generation of Axisymmetric Mode Jet Screech Tones," *AIAA Journal*, Vol. 36, No. 10, 1998, pp. 1801–1807.
- <sup>12</sup>Powell, A., "Theory of Vortex Sound," *Journal of the Acoustical Society of America*, Vol. 36, No. 1, 1964, pp. 177–195.
- <sup>13</sup>Mitchell, B. E., Lele, S. K., and Moin, P., "Direct Computation of the Sound from a Compressible Co-Rotating Vortex Pair," *Journal of Fluid Mechanics*, Vol. 285, 1995, pp. 181–202.
- <sup>14</sup>Brown, G. L., and Roshko, A., "On Density Effects and Large Structure in Turbulent Mixing Layers," *Journal of Fluid Mechanics*, Vol. 64, No. 4, 1974, pp. 775–816.
- <sup>15</sup>Winant, C. D., and Browand, F. K., "Vortex Pairing: The Mechanism of Turbulent Mixing Layer Growth at Moderate Reynolds Number," *Journal of Fluid Mechanics*, Vol. 63, No. 2, 1974, pp. 237–255.
- <sup>16</sup>Wyganski, I., Oster, D., Fiedler, H., and Dziomba, B., "Perseverance of a Quasi-Two-Dimensional Eddy-Structure," *Journal of Fluid Mechanics*, Vol. 93, 1979, pp. 325–335.
- <sup>17</sup>Ho, C. M., and Huang, L. S., "Subharmonics and Vortex Merging in Mixing Layers," *Journal of Fluid Mechanics*, Vol. 119, 1982, pp. 443–473.
- <sup>18</sup>Tam, C. K. W., and Webb, J. C., "Dispersion-Relation-Preserving Finite Difference Schemes for Computational Acoustics," *Journal of Computational Physics*, Vol. 107, Aug. 1993, pp. 262–281.
- <sup>19</sup>Hu, F. Q., Hussaini, M. Y., and Manthey, J. L., "Low-Dissipation and Low-Dispersion Runge–Kutta Schemes for Computational Acoustics," *Journal of Computational Physics*, Vol. 124, Jan. 1996, pp. 177–191.
- <sup>20</sup>Stanley, S., and Sarkar, S., "Simulations of Spatially Developing Two-Dimensional Shear Layers and Jets," *Theoretical and Computational Fluid Dynamics*, Vol. 9, No. 2, 1997, pp. 121–147.
- <sup>21</sup>Tam, C. K. W., and Dong, Z., "Radiation and Outflow Boundary Conditions for Direct Computation of Acoustic and Flow Disturbances in a Nonuniform Mean Flow," *Journal of Computational Acoustics*, Vol. 4, No. 2, 1996, pp. 175–201.
- <sup>22</sup>Hixon, R., Shih, S. H., and Mankbadi, R. R., "Evaluation of Boundary Conditions for Computational Aeroacoustics," *AIAA Journal*, Vol. 33, No. 11, 1995, pp. 2006–2012.
- <sup>23</sup>Hardin, J. C., Ristorcelli, J. R., and Tam, C. K. W. (eds.), *Workshop on Benchmark Problems in Computational Aeroacoustics*, NASA CP-3300, 1995, pp. 1–14.
- <sup>24</sup>Colonus, T., Lele, S. K., and Moin, P., "Boundary Conditions for Direct Computation of Aerodynamic Sound Generation," *AIAA Journal*, Vol. 31, No. 9, 1993, pp. 1574–1582.
- <sup>25</sup>Bérenger, J.-P., "A Perfectly Matched Layer for the Absorption of Electromagnetic Waves," *Journal of Computational Physics*, Vol. 114, No. 2, 1994, pp. 185–200.
- <sup>26</sup>Smagorinsky, J. S., "General Circulation Experiments with the Primitive Equations: I. The Basic Experiment," *Monthly Weather Review*, Vol. 91, No. 3, 1963, pp. 99–163.
- <sup>27</sup>Germano, M., Piomelli, U., Moin, P., and Cabot, W. H., "A Dynamic Subgrid-Scale Eddy Viscosity Model," *Physics of Fluids A*, Vol. 3, No. 7, 1991, pp. 1760–1765.
- <sup>28</sup>Erlebacher, G., Hussaini, M. Y., Speziale, C. G., and Zang, T. A., "Toward the Large-Eddy Simulation of Compressible Turbulent Flows," *Journal of Fluid Mechanics*, Vol. 238, 1992, pp. 155–185.
- <sup>29</sup>Crow, S. C., and Champagne, F. H., "Orderly Structure in Jet Turbulence," *Journal of Fluid Mechanics*, Vol. 48, No. 3, 1971, pp. 547–591.
- <sup>30</sup>Michalke, A., "On the Inviscid Instability of the Hyperbolic-Tangent Velocity Profile," *Journal of Fluid Mechanics*, Vol. 19, 1964, pp. 543–556.
- <sup>31</sup>Bogey, C., "Calcul direct du bruit aérodynamique, et validation de modèles hybrides," Ph.D. Dissertation, Ecole Centrale de Lyon, Ecully, France, April 2000.
- <sup>32</sup>Hussain, A. K. M. F., "Coherent Structures—Reality and Myth," *Physics of Fluids*, Vol. 26, No. 10, 1983, pp. 2816–2850.
- <sup>33</sup>Crighton, D., "Basic Principles of Aerodynamic Noise Generation," *Progress in Aerospace Sciences*, Vol. 16, No. 1, 1975, pp. 31–96.
- <sup>34</sup>Sarkar, S., and Hussaini, Y., "Computation of the Acoustic Radiation from Bounded Homogeneous Flows," *Computational Aeroacoustics*, edited by J. C. Hardin and M. Y. Hussaini, Springer-Verlag, New York, 1993, pp. 335–355.

P. J. Morris  
Associate Editor